

Geophysical Research Letters

RESEARCH LETTER

10.1029/2019GL082621

Key Points:

- We present laboratory measurements of far-field large-amplitude whistler mode pulse generated by impulsive magnetic reconnection event
- New multicluster magnetic probe can characterize wave dispersion from a single shot using analysis techniques from formation spacecraft
- Large-amplitude whistler waves from impulsive reconnection provide an additional particle acceleration mechanism for solar flares

Supporting Information:

- Supporting Information S1

Correspondence to:

M. A. Haw,
mhaw@alumni.caltech.edu

Citation:

Haw, M. A., Seo, B., & Bellan, P. M. (2019). Laboratory measurement of large-amplitude whistler pulses generated by fast magnetic reconnection. *Geophysical Research Letters*, 46, 7105–7112. <https://doi.org/10.1029/2019GL082621>




Received 1 MAR 2019

Accepted 10 JUN 2019

Accepted article online 18 JUN 2019

Published online 1 JUL 2019

Laboratory Measurement of Large-Amplitude Whistler Pulses Generated by Fast Magnetic Reconnection

Magnus A. Haw¹ , Byonghoon Seo¹ , and Paul M. Bellan¹ 

¹Applied Physics, California Institute of Technology, Pasadena, CA, USA

Abstract We present observations of large-amplitude ($\delta B/B \sim 0.01$) oblique whistler wave pulses generated by a spontaneous, 3-D localized magnetic reconnection event in the Caltech jet experiment. The wave pulses are measured more than 50 ion skin depths from the reconnection location by a tetrahedron array of three-axis B-dot probes that mimic the pyramid flight formations of the Cluster and Magnetospheric Multiscale Mission spacecraft. Measurements of background parameters, wave polarization, and wave dispersion confirm that the pulses are whistler modes. These results demonstrate that localized impulsive reconnection events can generate large-amplitude, oblique whistler wave pulses that propagate far outside the reconnection region. This provides a new pathway for the generation of magnetospheric whistler pulses and may help explain relativistic particle acceleration in phenomena such as solar flares that incorporate 3-D localized impulsive magnetic reconnection.

1. Introduction

Magnetic reconnection governs changes in magnetic topology by which magnetic energy converts to kinetic energy in a thin boundary layer. Typical signatures of reconnection include X-rays, localized heating, and magnetized waves. This process is considered to be responsible for large impulsive releases of energy in solar flares, magnetic storms in Earth's magnetotail, disruptions in fusion devices, and laboratory circumstances simulating these solar and space plasmas (Cassak et al., 2008; Gekelman et al., 2018; Marshall et al., 2018; Moser & Bellan, 2012; Priest & Forbes, 2000; Xiao et al., 2010; Yamada et al., 2016). In these systems, the collisionless reconnection rate is typically orders of magnitude faster than resistive reconnection (Brown et al., 2006; Øieroset et al., 2001; Yamada et al., 2006). Spacecraft (Eastwood et al., 2006; Le et al., 2009), laboratory (Ren et al., 2005), analytic (Bellan, 2014), and simulation (Cassak et al., 2005) results indicate that the Hall effect, in particular, is important in accelerating the reconnection rate.

Whistlers are the characteristic modes present in Hall-mediated reconnection due to the spatial and temporal scales involved (Bellan, 2014; Rogers et al., 2001; Shay et al., 2002; Singh, 2013; Yoon & Bellan, 2017). These waves have been observed in conjunction with collisionless reconnection events in the magnetosphere (Graham et al., 2015; Huang et al., 2016; Wilder et al., 2016) and laboratory experiments (Gekelman & Stenzel, 1984; Ji et al., 2004). Large-amplitude whistler pulses ($\delta B/B \sim 0.01$) are a class of whistler wave with significantly higher amplitude than the majority of whistler modes observed in the magnetosphere ($\delta B/B \ll 0.001$) (Van Compernelle et al., 2015). These pulses are considered an essential driver of magnetospheric electron energization and electron loss (Artemyev et al., 2016; Breneman et al., 2017; Cattell et al., 2008), because they can efficiently accelerate electrons to relativistic energies (Artemyev et al., 2016; Mourenas et al., 2018; Yoon, 2011; Yoon et al., 2013). There are two known mechanisms for generating large-amplitude whistler pulses: kinetic velocity space inhomogeneities (i.e., electron beams; Brenning et al., 2017; Sauer & Sydora, 2010) and fluid/topological inhomogeneities (i.e. inductive antennas, x points; Stenzel et al., 2006; Yoon & Bellan, 2017). However, it is not yet clear to what degree each mechanism contributes to the whistlers observed during collisionless reconnection.

Previous experimental observations of whistlers generated by magnetic reconnection are localized to the reconnection current layer. Gekelman and Stenzel (1984) measured whistlers inside a reconnection current layer in the Magnetic Field Line Reconnection Experiment at UCLA. Ji et al. (2004) measured large-amplitude whistlers inside the MRX reconnection layer. von Stechow et al. (2015) also identified whistlers in the current layer of the Vineta II reconnection experiment. These previous experiments all identify similar whistler fluctuations inside the current sheet, identify right-handed polarization, and use phase

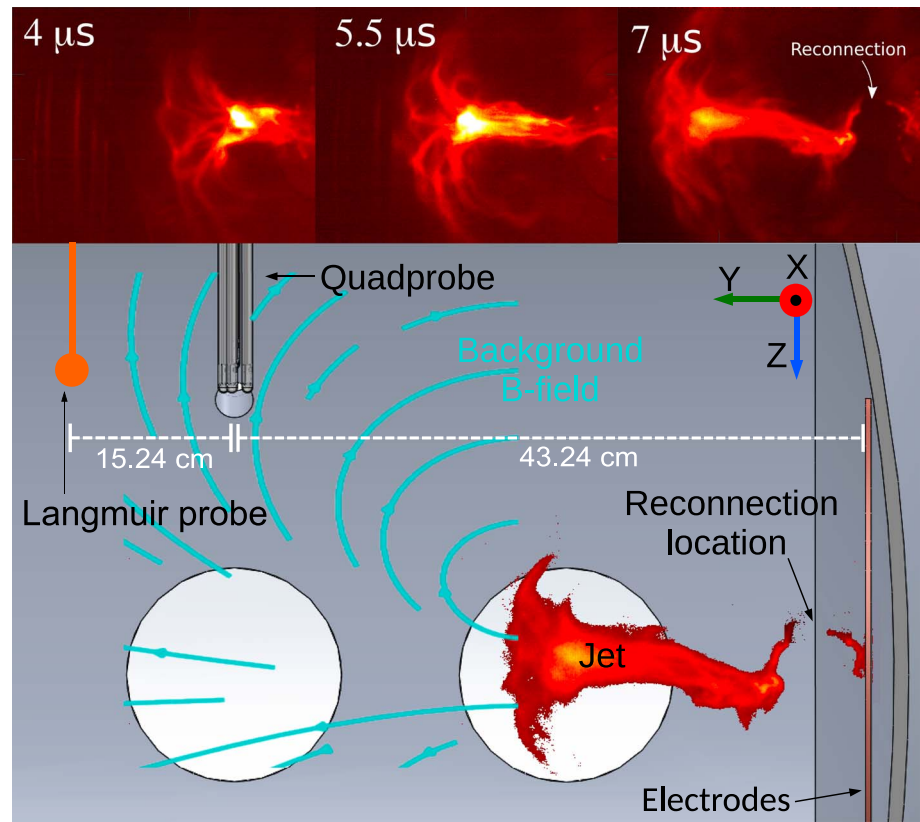


Figure 1. (top) Visible light images of jet evolution and detachment over time recorded by a fast movie camera. Reconnection event from axis breaking is visible in 7 μs frame. (bottom) Plot showing the quadprobe and Langmuir probe locations relative to the reconnection location and the background poloidal B-field. Axes are defined such that \hat{y} is the axial direction, \hat{z} is vertically down, and \hat{x} is out of the page. The jet moves axially at a velocity of 50–70 km/s.

differences between two probes to estimate the wave vector magnitude. However, there have been no previous laboratory measurements of whistlers far from the reconnection region or measurements with sufficient spatial resolution to resolve the wave vector in 3-D.

This paper reports the first far-field (>50 ion skin depths) wave vector measurements of large-amplitude whistler wave pulses ($0.001 \leq \delta B/B \leq 0.05$) generated by impulsive magnetic reconnection events. The wave pulses are measured in the Caltech jet experiment (Chai et al., 2016; Hsu & Bellan, 2002) with a new multicluster \hat{B} -probe mimicking the tetrahedral formations of the Cluster (Dunlop et al., 2001; Eastwood et al., 2006; Graham et al., 2015) and Magnetospheric Multiscale Mission (MMS) spacecraft (Breuillard et al., 2016; Cao et al., 2017; Gershman et al., 2017; Wilder et al., 2016). This tetrahedral set of clusters allows measurement of the 3-D wave vector and the dispersion relation using data from a single shot and will be subsequently referred to as the “quadprobe.” These results demonstrate that impulsive reconnection events can generate large-amplitude whistler pulses which can propagate far from the reconnection location. These results are relevant to large-amplitude whistlers observed in the magnetosphere and may help explain relativistic particle acceleration in other systems with impulsive magnetic reconnection such as solar flares.

2. Experimental Setup

The Caltech jet experiment launches a magnetohydrodynamic-driven collimated jet with a dense central axis (Figure 1). As the axis lengthens, a combination of instabilities induces a fast detachment event where the axis breaks off from the electrodes.

The apparatus consists of a planar coaxial magnetized plasma gun with three primary subsystems: a gas supply system, a bias coil for background poloidal magnetic field, and a capacitor bank to drive current between the electrodes. Plasma is generated in a specific series of steps: (1) Gas is puffed in from eight pairs of

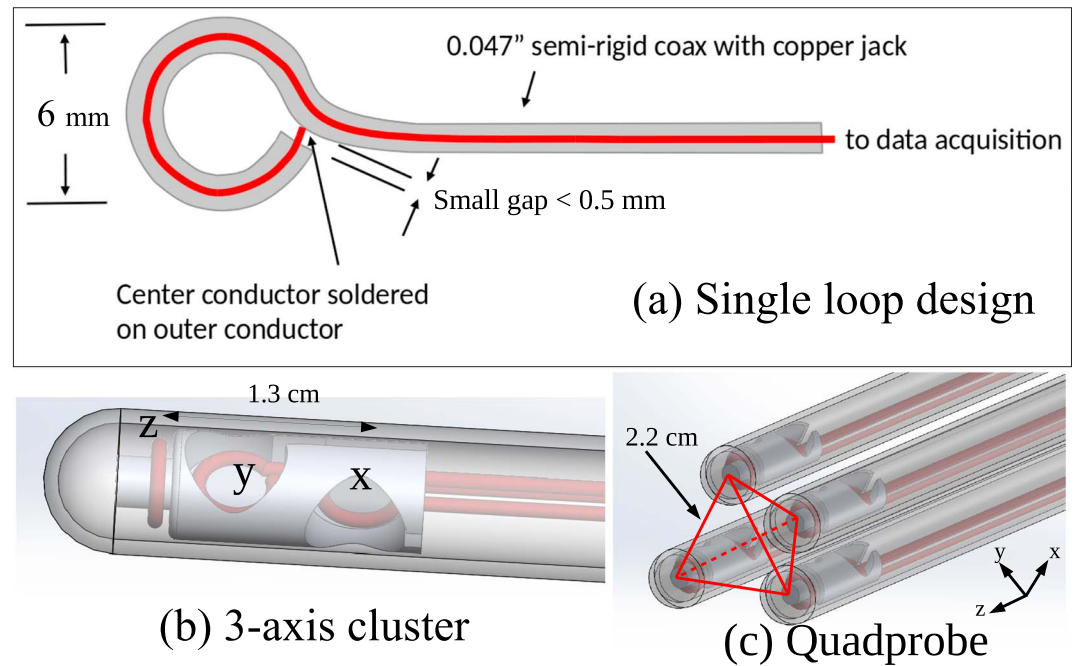


Figure 2. (a) Single-loop \hat{B} -probe design from Zhai (2015). (b) The 3-D clusters are formed from three mutually perpendicular loops glued to a plastic mounting piece. (c) The quadprobe is constructed from four clusters arranged in a tetrahedron with side length 2.2 cm. The probe coordinate system is shown at the bottom right corner.

concentric nozzles on the inner disk and outer annulus electrodes, (2) a poloidal background magnetic field is generated by the coil behind the electrodes, and (3) the capacitor bank is switched across the electrodes, breaking down the neutral gas to form plasma. Due to the concentric arrangement of the gas nozzles and the poloidal magnetic field, the plasma breaks down along eight radial arches between the inner and outer electrodes. These plasma arches merge along the central axis and expand over time (see Figure 1). These initial stages of jet evolution are very reproducible with $\sim 10\%$ shot to shot variation. As the arches expand, the central axis lengthens and develops a helical instability, the Kruskal-Shafranov kink instability (Hsu & Bellan, 2003). Since the current and the background magnetic field are antiparallel in the axial direction, the jet kinks in a left-handed sense (Hsu & Bellan, 2003). The apparatus is described in detail in Hsu and Bellan (2002), Moser and Bellan (2012), and Chai et al. (2016), and a 3-D magnetohydrodynamic simulation of the experiment is described in Zhai et al. (2014). During the fast lateral acceleration of the growing helical perturbation, a secondary Rayleigh-Taylor instability develops on the trailing edge of the laterally moving jet. The fast growth of the Rayleigh-Taylor ripples results in the jet breaking and detaching from the electrodes (Moser & Bellan, 2012; Zhai & Bellan, 2016). This detachment necessarily involves a magnetic reconnection event due to the changing magnetic topology. Previous measurements of detachment events (Chai et al., 2016; Marshall et al., 2018) identified simultaneous emission of extreme ultraviolet light, X-rays, current disruptions, and broadband magnetic oscillations near the reconnection site. These reconnection events are not as reproducible as the global jet morphology, and occur for $\sim 60\%$ of shots taken with a particular set of initial conditions. Due to the significant variation in reconnection location, timing, and orientation, the emitted wave fields must be characterized in individual shots.

3. Quadprobe Design

The quadprobe has four three-axis clusters of \hat{B} -probes for a total of 12 individual channels. Each channel or \hat{B} -probe is a single-turn loop (3-mm radius) constructed from 1.2-mm semirigid coaxial cable (Figure 2a). One stripped end of the coax is bent in a circle and, at the point where the endpoint intersects the main axis, the center conductor is electrically connected to the outer conductor to complete the circuit. Three of these loops are arranged along perpendicular axes to create a 3-D cluster (Figure 2b). The coaxial loop design is based on the work of Zhai (2015) and provides electrostatic shielding and linear frequency response up to several hundred megahertz. Each loop is connected to a 100-MHz digitizer by a 12-m-long semirigid coax

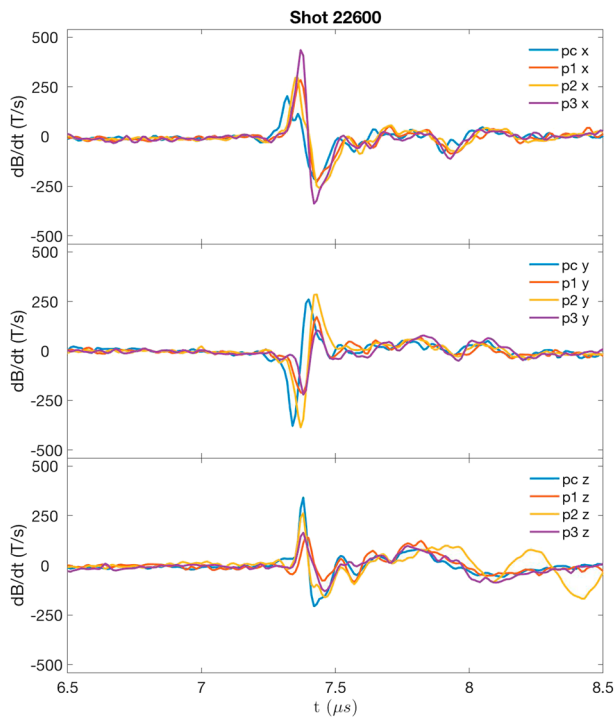


Figure 3. Plots of (top) \vec{B}_x , (middle) \vec{B}_y , and (bottom) \vec{B}_z at each probe cluster for shot #22600 filtered in the range of 0.5 to 20 MHz.

less than $1 \mu\text{s}$ with frequencies between 3 and 10 MHz. To bound the plasma density at the probe location, Langmuir probe measurements were taken, 15.24 cm ($6''$) downstream of the quadprobe on a sample of 50 separate shots. These measurements give electron densities between 0.6×10^{17} and $1.4 \times 10^{17} \text{ m}^{-3}$ and electron temperatures between 10 and 30 eV. The density at the quadprobe is estimated to be in the range $0.9\text{--}2.8 \times 10^{17} \text{ m}^{-3}$ by interpolating between these Langmuir measurements and upstream density measurements from a translatable interferometer (Seo & Bellan, 2017). Thus, the upper bound on the Alfvén velocity in the vicinity of the quadprobe is $v_A = 1.5 \times 10^5 \text{ m/s}$ ($|B| = 0.002 \text{ T}$, $n = 0.9 \times 10^{17}$). This is slightly faster than the Alfvén speed along the jet axis $v_A \leq 10^5 \text{ m/s}$, where the magnetic field and density are orders of magnitude larger ($|B| \sim 0.1 \text{ T}$, $n \sim 10^{21}$).

4.2. Pulse Wave Classification

The pulse is identified as a wave from the propagation speed for the following reasons. Time of flight delays between clusters ($< 30 \text{ ns}$) indicate that the pulse is traveling faster than $5 \times 10^5 \text{ m/s}$ in the vicinity of the probes, that is, many times faster than the upper bound on the Alfvén speed in the vicinity of the probes. The maximum observed velocity of features in the jet is less than the local average Alfvén speed $v_A \approx 10^5 \text{ m/s}$ as determined by volumetric magnetic field measurements, interferometry and visible light images. If the fluctuations were produced by coherent structures ejected during reconnection and traveling at the local Alfvén speed, such structures would arrive at the probe at $16 \pm 3 \mu\text{s}$, that is, long after the wave pulses are observed. Thus, the signal observed at the quadprobe could not be a coherent bulk structure ejected during reconnection since such a structure would have to travel at the Alfvén speed or slower. The time for a pulse to resistively diffuse 50 cm in a 2- to 20-eV plasma is $L^2 \mu_0 / \eta \geq 2 \times 10^{-3} \text{ s}$ which is orders of magnitude longer than the duration of the experiment. The signal thus could not be the result of resistive diffusion. The signal propagation is therefore too fast to be either a coherent bulk structure ejected via reconnection or a diffusive pulse and instead is consistent with wave propagation.

The pulse parameters are also within the whistler region on a CMA diagram: The pulse frequency range (3–10 MHz) is (i) below the electron plasma frequency ($\sim 3 \text{ GHz}$), (ii) below the electron cyclotron frequency (28–56 MHz), and (iii) above the lower hybrid frequency (0.6–1.3 MHz). The group velocity of whistler modes in this parameter space is $1.2\text{--}5 \times 10^6 \text{ m/s}$, which is consistent with the observed propagation speed.

cable that is linked by two ferrite beads (core type 31, $n = 4$ turns) which attenuate spurious common mode electric and magnetic pickup in the range 1–300 MHz. These ferrites provide 90 dB of noise attenuation (i.e., a factor of $10^{4.5}$) relative to an unshielded loop attached to a RG-58 BNC cable.

4. Wave Measurements

High-frequency magnetic pulses were observed by the quadprobe concurrently with visible detachment of the hydrogen jet in visible light images. These pulses are determined to be whistler waves on the basis of the pulse speed, measurements of the background plasma parameters, the wave polarization, and comparisons with the whistler dispersion relation. The coordinate system is defined relative to the quadprobe orientation as shown in Figure 2c so the jet is moving in the y direction.

Figure 3 shows the raw signals from all quadprobe channels for a wave pulse observed in shot #22600. The \vec{B} fluctuations indicate that the wave passes at 7.3–7.6 μs at which time the detachment of the jet column is visible in Figure 1. Each channel is digitized at 12-bit resolution at a frequency of 100 MHz.

4.1. Pulse Parameters

During the pulses, the background magnetic field at the quadprobe location maintains a nearly constant value between 0.001 and 0.002 T and points in the negative x-z direction with $\vec{B} \approx [-0.6\hat{x}, -0.1\hat{y}, -0.8\hat{z}]$ (coordinate system given in Figures 1 and 2). The pulses have a duration of

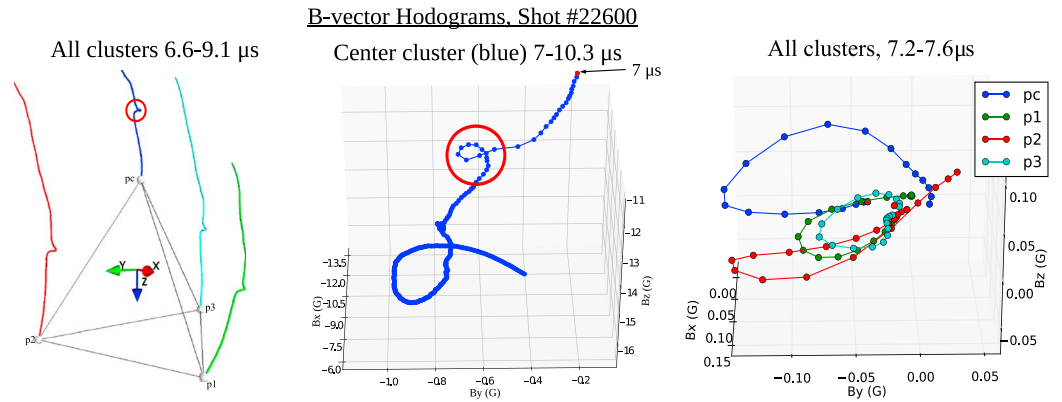


Figure 4. (left) Plot of B -field hodograms for all four clusters where each path is started at the respective cluster position indicated by a white sphere. The high-frequency first period of the wave pulse is circled in red for the center cluster. This feature is also visible for the other three clusters. (middle) Detailed hodogram of center cluster for shot #22600 (z axis orientation is flipped relative to adjacent plot). This time frame can be compared with the x component plotted in Figure 3. (right) Zoom-in view of the circled region in adjacent plots with background field subtracted. All clusters exhibit rotation in nearly the same plane.

Further comparisons with group velocity are discussed in section 5 after calculating the pulse's dispersion relation.

4.3. Pulse Polarization

The wave pulses are confirmed to have right-handed circular polarization, consistent with whistler mode propagation. The wave polarization is traditionally visualized using a plot called a hodogram (Urrutia & Stenzel, 2014), which plots $\mathbf{B}(t)$ as a path in 3-D space. Helical or circular motion of hodogram paths indicate circular polarization. Figure 4 plots hodograms for shot #22600 for all four probes (left), for a single probe (middle), and a zoomed version for all probes (right) showing right-handed polarization. Cluster $p2$'s hodogram has a more elongated shape than the other clusters, which could be due to shadowing effects/reflections from the other probes as it is furthest from the wave source.

4.4. Pulse Statistics

Out of 51 shots, 31 had visible signs of reconnection and high-frequency magnetic perturbations were measured in 23 of these 31 shots. The pulses perturb the background B -field at the probe location by an average of 1.2% with a standard deviation of 1%. More violent visible detachment events are also associated with stronger wave pulses. The strongest observed pulse generated a 5% perturbation of the background field. In the other 20 shots with no visible signs of reconnection, no high-frequency perturbations were observed. Additional images and plots showing the typical reconnection and nonreconnecting modes are provided in the supporting information. The absence of wave pulses in shots without visible reconnection provides strong evidence that the observed wave pulses are produced during the reconnection events. If the wave pulses were generated by a different mechanism, then pulses should have been observed during shots where visible reconnection does not occur.

5. Calculation of $\mathbf{k}(\omega)$

The dispersion relation $\mathbf{k}(\omega)$ for individual wave pulses can be extracted from the quadprobe measurements using a new method described by Bellan (2016). This method calculates the wave vector from cospatial measurements of the wave $\tilde{\mathbf{B}}$ and $\tilde{\mathbf{J}}$. This calculation assumes that the displacement current is negligible (i.e., quasi-neutral plasma, $\mathbf{k} \cdot \tilde{\mathbf{J}} = 0$) and that there are no standing waves. In this regime, the pre-Maxwell Ampere's Law for the wave $\tilde{\mathbf{B}}$ and $\tilde{\mathbf{J}}$ can be written as

$$\mu_0 \tilde{\mathbf{J}} = i\mathbf{k} \times \tilde{\mathbf{B}}. \quad (1)$$

This implies $\tilde{\mathbf{J}} \perp \mathbf{k}$, $\tilde{\mathbf{B}}$ and since $\mathbf{k} \cdot \tilde{\mathbf{B}} = 0$, the three vectors form an orthogonal basis in Fourier space. Solving for \mathbf{k} gives,

$$\mathbf{k}(\omega) = i\mu_0 \frac{\tilde{\mathbf{J}}(\omega) \times \tilde{\mathbf{B}}^*(\omega)}{\tilde{\mathbf{B}}(\omega) \cdot \tilde{\mathbf{B}}^*(\omega)}. \quad (2)$$

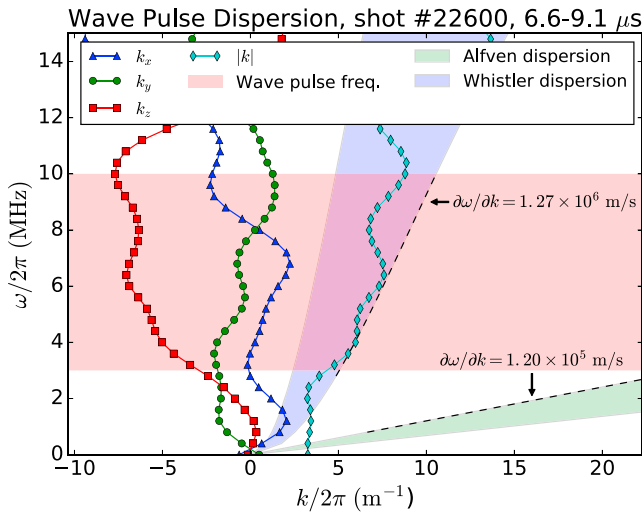


Figure 5. Plot of wave vector components and magnitude (k_x , k_y , k_z , $|k|$) calculated from the wave pulse in shot #22600, $|B| = 16.5$ G. The pink region (3–10 MHz) indicates the wave pulse frequency range and $|k|$ in this region corresponds to a wavelength of 12–16 cm. The wave vector components show that the pulse is propagating nearly in the $-\hat{z}$ direction. The Alfvén and whistler dispersions are shown as green and blue regions, respectively, for densities $(0.9\text{--}2.8 \times 10^{17})$, oblique propagation ($30\text{--}60^\circ$). Group velocities are shown as dotted lines. The measured dispersion in the 3- to 10-MHz band is consistent with the theoretical whistler dispersion.

Bellan (2016) also provides an alternative solution to equation (2) using cross-correlation functions. This k-vector method has been previously used on MMS data to evaluate wave-particle energy exchange (Gershman et al., 2017).

\vec{B} and \vec{J} can both be calculated at the center of the quadprobe by writing the magnetic field at each cluster location B_i as the Taylor expansion of B_c at the tetrahedron center,

$$B_i = B_c + (\vec{\nabla} B_c) \cdot R_i, \quad (3)$$

where the i subscript denotes a probe index and R_i is the probe location relative to the center of the tetrahedron. Then, equation (3) can be inverted (see supporting information) to obtain B_c and $\vec{\nabla} B_c$. The current density at the tetrahedron center J_c can be calculated from the components of $\vec{\nabla} B_c$. This calculation of current density from a tetrahedral set of magnetic measurements is known as the “curlometer” technique and has been regularly used on the Cluster and MMS spacecraft formations (Dunlop et al., 2001; Gershman et al., 2017).

Using this curlometer technique, cospatial \vec{B} and \vec{J} are calculated at the center of the quadprobe from filtered data (1–20 MHz third-order Butterworth filter) from the four B clusters. Then the dispersion relation is calculated using equation (2). Figure 5 plots the measured wave vector dispersion for shot #22600 against the theoretical whistler and Alfvén dispersion for densities $n = 0.9\text{--}2.8 \times 10^{17}$ and $|B| = 16.5$ G. For the dominant frequencies in the pulse (6–9 MHz), the wave vector magnitude is $40\text{--}50$ m^{-1} corresponding to a wavelength of 12–16 cm. The wave vector is propagating nearly in the negative \hat{z} direction, oblique ($30^\circ < \theta < 60^\circ$)

relative to the background magnetic field. As seen in Figure 1, the negative \hat{z} direction corresponds to propagation away from the reconnection location. The average wave vector for the 11 pulses with $\delta B/B > 0.01$ follows the same trends (see supporting information).

Fitting the measured dispersion to the theoretical whistler wave dispersion, gives a density of $2.5 \times 10^{17} \text{ m}^{-3}$ and a propagation velocity of $1.6 \times 10^{17} \text{ m/s}$ for 30° oblique propagation. For the shot shown in Figure 5, the maximum Alfvén group velocity ($\partial\omega/\partial k_A = 1.2 \times 10^5$, shown as dotted line) is 13 times smaller than the measured group velocity. This is consistent with the discussion in section 4.2, which identified the pulses as a whistler mode from a propagation speed much greater than the local Alfvén speed.

6. Discussion

The results characterize isolated wave pulses on the Caltech jet experiment produced by fast reconnection of the jet axis. The magnetic measurements are acquired using a new multicluster tetrahedral probe motivated by the Cluster and MMS spacecraft formations. This probe, in conjunction with a new wave vector extraction technique, is able to obtain both the 3-D wave vector and dispersion relation of individual wave pulses from single shot measurements. The measured propagation speed, dispersion, and right-hand circular polarization indicate that the pulses are whistler mode waves.

These observations demonstrate that localized, impulsive reconnection can generate large-amplitude whistler pulses that can propagate a significant distance (>50 ion skin depths) from the reconnection region. These isolated, coherent pulses more closely resemble large-amplitude whistler spheromaks generated by inductive loop antennas (Stenzel et al., 2006) than the broadband fluctuations generated by electron beams (Brenning et al., 2017). This is consistent with the understanding that the impulsive reconnection of the jet causes an abrupt change in both the magnetic field and current, and so acts as an antenna (Yoon & Bellan, 2018). Consequently, these pulses are more likely generated by a fluid mechanism than a kinetic one. These pulses may also be relevant to solar flares as they are observed in conjunction with high-energy photons during localized, impulsive magnetic reconnection events. If similar large-amplitude whistler pulses are generated during flare reconnection, then these pulses could provide an efficient mechanism for accelerating electrons to relativistic energies (Yoon, 2011). This could potentially resolve the flare particle number

problem (Benz, 2016) by providing a mechanism for electron acceleration over a much larger region than the reconnection volume.

Acknowledgments

This material is based upon work supported by the NSF/DOE Partnership in Plasma Science and Engineering via U.S. Department of Energy Office of Science, Office of Fusion Energy Sciences award DE-FG02-04ER54755, by the Air Force Office of Scientific Research Space Science Program via award FA9550-11-1-0184, and by the NSF SHINE program via award 1348393. The associated data files and analysis scripts for this paper are available here: github.com/magnus-haw/whistler-pulses.

References

Artemyev, A., Agapitov, O., Mourenas, D., Krasnoselskikh, V., Shastun, V., & Mozer, F. (2016). Oblique whistler-mode waves in the Earth's inner magnetosphere: Energy distribution, origins, and role in radiation belt dynamics. *Space Science Reviews*, 200(1), 261–355. <https://doi.org/10.1007/s11214-016-0252-5>

Bellan, P. M. (2014). Fast, purely growing collisionless reconnection as an eigenfunction problem related to but not involving linear whistler waves. *Physics of Plasmas*, 21(10), 102108. <https://doi.org/10.1063/1.4897375>

Bellan, P. M. (2016). Revised single-spacecraft method for determining wave vector *k* and resolving space-time ambiguity. *Journal of Geophysical Research: Space Physics*, 121, 8589–8599. <https://doi.org/10.1002/2016JA022827>

Benz, A. O. (2016). Flare observations. *Living Reviews in Solar Physics*, 14(1), 2. <https://doi.org/10.1007/s41116-016-0004-3>

Breneman, A. W., Crew, A., Sample, J., Klumpp, D., Johnson, A., Agapitov, O., et al. (2017). Observations directly linking relativistic electron microbursts to whistler mode chorus: Van Allen Probes and FIREBIRD II. *Geophysical Research Letters*, 44, 11,265–11,272. <https://doi.org/10.1002/2017GL075001>

Brenning, N., Axns, I., Koepke, M., Raadu, M. A., & Tennfors, E. (2017). Radiation from an electron beam in magnetized plasma: Excitation of a whistler mode wave packet by interacting, higher-frequency, electrostatic-wave eigenmodes. *Plasma Physics and Controlled Fusion*, 59(12), 124006. <https://doi.org/10.1088/1361-6587/aa941b>

Breuillard, H., Le Contel, O., Retino, A., Chasapis, A., Chust, T., Mirioni, L., et al. (2016). Multispacecraft analysis of dipolarization fronts and associated whistler wave emissions using MMS data. *Geophysical Research Letters*, 43, 7279–7286. <https://doi.org/10.1002/2016GL069188>

Brown, M. R., Cothran, C. D., & Fung, J. (2006). Two fluid effects on three-dimensional reconnection in the Swarthmore Spheromak Experiment with comparisons to space data. *Physics of Plasmas*, 13(5), 56503. <https://doi.org/10.1063/1.2180729>

Cao, D., Fu, H. S., Cao, J. B., Wang, T. Y., Graham, D. B., Chen, Z. Z., et al. (2017). MMS observations of whistler waves in electron diffusion region. *Geophysical Research Letters*, 44, 3954–3962. <https://doi.org/10.1002/2017GL072703>

Cassak, P. A., Mullan, D. J., Shay, M. A., & L69 (2008). From solar and stellar flares to coronal heating: Theory and observations of how magnetic reconnection regulates coronal conditions. *The Astrophysical Journal Letters*, 676. <https://doi.org/10.1086/587055>

Cassak, P. A., Shay, M. A., & Drake, J. F. (2005). Catastrophe model for fast magnetic reconnection onset. *Physical Review Letters*, 95(23), 235002. <https://doi.org/10.1103/PhysRevLett.95.235002>

Cattell, C., Wygant, J. R., Goetz, K., Kersten, K., Kellogg, P. J., von Rosenvinge, T., et al. (2008). Discovery of very large amplitude whistler-mode waves in Earth's radiation belts. *Geophysical Research Letters*, 35, L01105. <https://doi.org/10.1029/2007GL032009>

Chai, K.-B., Zhai, X., & Bellan, P. M. (2016). Extreme ultra-violet burst, particle heating, and whistler wave emission in fast magnetic reconnection induced by kink-driven Rayleigh-Taylor instability. *Physics of Plasmas*, 23(3), 32122. <https://doi.org/10.1063/1.4944390>

Dunlop, M. W., Balogh, A., Glassmeier, K.-H., & Robert, P. (2001). Four-point Cluster application of magnetic field analysis tools: The curlometer. *Journal of Geophysical Research*, 107(A11), 1384. <https://doi.org/10.1029/2001JA005088>

Eastwood, J. P., Phan, T., Mozer, F. S., Shay, M. A., Fujimoto, M., Retinó, A., et al. (2006). Multipoint observations of the Hall electromagnetic field and secondary island formation during magnetic reconnection. *Journal of Geophysical Research*, 112, A06235. <https://doi.org/10.1029/2006JA012158>

Gekelman, W., DeHaas, T., Pribyl, P., Vincena, S., Compernelle, B. V., Sydora, R., & Tripathi, S. K. P. (2018). Non-local Ohms law, plasma resistivity, and reconnection during collisions of magnetic flux ropes. *The Astrophysical Journal*, 853(1), 33. <https://doi.org/10.3847/1538-4357/aa9fec>

Gekelman, W., & Stenzel, R. L. (1984). Magnetic field line reconnection experiments: 6. Magnetic turbulence. *Journal of Geophysical Research*, 89(A5), 2715–2733. <https://doi.org/10.1029/JA089iA05p02715>

Gershman, D. J., F-Vias, A., Dorelli, J. C., Boardsen, S. A., Avannov, L. A., Bellan, P. M., et al. (2017). Wave-particle energy exchange directly observed in a kinetic Alfvén-branch wave. *Nature Communications*, 8, 14719. <https://doi.org/10.1038/ncomms14719>

Graham, D. B., Vaivads, A., Khotyaintsev, Y. V., & André, M. (2015). Whistler emission in the separatrix regions of asymmetric magnetic reconnection. *Journal of Geophysical Research: Space Physics*, 121(3), 1934–1954. <https://doi.org/10.1002/2015JA021239>

Hsu, S. C., & Bellan, P. M. (2002). A laboratory plasma experiment for studying magnetic dynamics of accretion discs and jets. *Monthly Notices of the Royal Astronomical Society*, 334, 257–261. <https://doi.org/10.1046/j.1365-8711.2002.05422.x>

Hsu, S. C., & Bellan, P. M. (2003). Experimental identification of the kink instability as a poloidal flux amplification mechanism for coaxial gun spheromak formation. *Physical Review Letters*, 90(21), 215002. <https://doi.org/10.1103/PhysRevLett.90.215002>

Huang, S. Y., Yuan, Z. G., Sahrquai, F., Fu, H. S., Pang, Y., Zhou, M., et al. (2016). Occurrence rate of whistler waves in the magnetotail reconnection region. *Journal of Geophysical Research: Space Physics*, 122, 7188–7196. <https://doi.org/10.1002/2016JA023670>

Ji, H., Terry, S., Yamada, M., Kulsrud, R., Kuritsyn, A., & Ren, Y. (2004). Electromagnetic fluctuations during fast reconnection in a laboratory plasma. *Physical Review Letters*, 92, 115001. <https://doi.org/10.1103/PhysRevLett.92.115001>

Le, A., Egedal, J., Daughton, W., Drake, J. F., Fox, W., & Katz, N. (2009). Magnitude of the Hall fields during magnetic reconnection. *Geophysical Research Letters*, 37, L03106. <https://doi.org/10.1029/2009GL041941>

Marshall, R. S., Flynn, M. J., & Bellan, P. M. (2018). Hard X-ray bursts observed in association with Rayleigh-Taylor instigated current disruption in a solar-relevant lab experiment. *Physics of Plasmas*, 25(11), 112101. <https://doi.org/10.1063/1.5054927>

Moser, A. L., & Bellan, P. M. (2012). Magnetic reconnection from a multiscale instability cascade. *Nature*, 482, 379–381. <https://doi.org/10.1038/nature10827>

Mourenas, D., Zhang, X.-J., Artemyev, A. V., Angelopoulos, V., Thorne, R. M., Bortnik, J., et al. (2018). Electron nonlinear resonant interaction with short and intense parallel chorus wave packets. *Journal of Geophysical Research: Space Physics*, 123, 4979–4999. <https://doi.org/10.1029/2018JA025417>

Oieroset, M., Phan, T. D., Fujimoto, M., Lin, R. P., & Lepping, R. P. (2001). In-situ detection of collisionless reconnection in the Earth's magnetotail. *Nature*, 412, 414–417. <https://doi.org/10.1038/35086520>

Priest, E., & Forbes, T. (2000). *Magnetic reconnection*. Cambridge, UK: Cambridge University Press. <https://doi.org/10.1017/CBO9780511525087>

Ren, Y., Yamada, M., Gerhardt, S., Ji, H., Kulsrud, R., & Kuritsyn, A. (2005). Experimental verification of the Hall effect during magnetic reconnection in a laboratory plasma. *Physical Review Letters*, 95, 55003. <https://doi.org/10.1103/PhysRevLett.95.055003>

- Rogers, B. N., Denton, R. E., Drake, J. F., & Shay, M. A. (2001). Role of dispersive waves in collisionless magnetic reconnection. *Physical Review Letters*, *87*, 195004. <https://doi.org/10.1103/PhysRevLett.87.195004>
- Sauer, K., & Sydora, R. D. (2010). Beam-excited whistler waves at oblique propagation with relation to STEREO radiation belt observations. *Annales Geophysicae*, *28*, 1,317–1,325. <https://doi.org/10.5194/angeo-28-1317-2010>
- Seo, B., & Bellan, P. M. (2017). Spatially translatable optical fiber-coupled heterodyne interferometer. *Review of Scientific Instruments*, *88*(12), 123504. <https://doi.org/10.1063/1.5007070>
- Shay, M. A., Drake, J. F., Swisdak, M., Dorland, W., & Rogers, B. N. (2002). Inherently three dimensional magnetic reconnection: A mechanism for bursty bulk flows? *Geophysical Research Letters*, *30*(6), 1345. <https://doi.org/10.1029/2002GL016267>
- Singh, N. (2013). Propagation and dispersion of whistler waves generated by fast reconnection onset. *Physics of Plasmas*, *20*(2), 22106. <https://doi.org/10.1063/1.4791650>
- Stenzel, R. L., Urrutia, J. M., & Strohmaier, K. D. (2006). Whistler modes with wave magnetic fields exceeding the ambient field. *Physical Review Letters*, *96*, 95004. <https://doi.org/10.1103/PhysRevLett.96.095004>
- Urrutia, J. M., & Stenzel, R. L. (2014). Magnetic antenna excitation of whistler modes. I. Basic properties. *Physics of Plasmas*, *21*(12), 122107. <https://doi.org/10.1063/1.4904354>
- Van Compernelle, B., An, X., Bortnik, J., Thorne, R. M., Pribyl, P., & Gekelman, W. (2015). Excitation of chirping whistler waves in a laboratory plasma. *Physical Review Letters*, *114*, 245002. <https://doi.org/10.1103/PhysRevLett.114.245002>
- von Stechow, A., Grulke, O., & Klingner, T. (2015). Experimental multiple-scale investigation of guide-field reconnection dynamics. *Plasma Physics and Controlled Fusion*, *58*(1), 14016. <https://doi.org/10.1088/0741-3335/58/1/014016>
- Wilder, F. D., Ergun, R. E., Goodrich, K. A., Goldman, M. V., Newman, D. L., Malaspina, D. M., & Holmes, J. C. (2016). Observations of whistler mode waves with nonlinear parallel electric fields near the dayside magnetic reconnection separatrix by the Magnetospheric Multiscale mission. *Geophysical Research Letters*, *43*, 5909–5917. <https://doi.org/10.1002/2016GL069473>
- Xiao, F., Zong, Q., Pu, Z., Su, Z., Cao, J., He, J., et al. (2010). Electron acceleration by whistler-mode waves around the magnetic null during 3D reconnection. *Plasma Physics and Controlled Fusion*, *52*(5), 52001.
- Yamada, M., Ren, Y., Ji, H., Breslau, J., Gerhardt, S., Kulsrud, R., & Kuritsyn, A. (2006). Experimental study of two-fluid effects on magnetic reconnection in a laboratory plasma with variable collisionality. *Physics of Plasmas*, *13*(5), 52119. <https://doi.org/10.1063/1.2203950>
- Yamada, M., Yoo, J., & Myers, C. E. (2016). Understanding the dynamics and energetics of magnetic reconnection in a laboratory plasma: Review of recent progress on selected fronts. *Physics of Plasmas*, *23*(5), 55402. <https://doi.org/10.1063/1.4948721>
- Yoon, P. H. (2011). Large-amplitude whistler waves and electron acceleration. *Geophysical Research Letters*, *38*, L12105. <https://doi.org/10.1029/2011GL047893>
- Yoon, Y. D., & Bellan, P. M. (2017). A generalized two-fluid picture of non-driven collisionless reconnection and its relation to whistler waves. *Physics of Plasmas*, *24*(5), 52114. <https://doi.org/10.1063/1.4982812>
- Yoon, Y. D., & Bellan, P. M. (2018). An intuitive two-fluid picture of spontaneous 2D collisionless magnetic reconnection and whistler wave generation. *Physics of Plasmas*, *25*(5), 55704. <https://doi.org/10.1063/1.5016345>
- Yoon, P. H., Pandey, V. S., & Lee, D.-H. (2013). Relativistic electron acceleration by oblique whistler waves. *Physics of Plasmas*, *20*(11), 112902. <https://doi.org/10.1063/1.4831965>
- Zhai, X. (2015). Experimental, numerical and analytical studies of the MHD-driven plasma jet, instabilities and waves (Doctoral dissertation, Caltech). Retrieved from <http://resolver.caltech.edu/CaltechTHESIS:06092015-162916583>
- Zhai, X., & Bellan, P. M. (2016). A hybrid Rayleigh-Taylor-current-driven coupled instability in a magnetohydrodynamically collimated cylindrical plasma with lateral gravity. *Physics of Plasmas*, *23*(3), 32121. <https://doi.org/10.1063/1.4943896>
- Zhai, X., Li, H., Bellan, P. M., & Li, S. (2014). Three-dimensional MHD simulation of the Caltech plasma jet experiment: First results. *The Astrophysical Journal*, *791*(1), 40. <https://doi.org/10.1088/0004-637X/791/1/40>